Electrochimica Acta 426 (2022) 140834

Contents lists available at ScienceDirect

Electrochimica Acta

journal homepage: www.journals.elsevier.com/electrochimica-acta

3-D inkjet printed solid oxide electrochemical reactors III. Cylindrical pillared electrode microstructures

N.M. Farandos, I. Jang *, J.C. Alexander, G.H. Kelsall #

Department of Chemical Engineering, Imperial College, London SW7 2AZ, UK

ARTICLE INFO

Keywords:
3D inkjet printing
Solid oxide fuel cells (SOFCs)
Yttria-stabilised zirconia (YSZ)
Pillared (YSZ) microstructures

ABSTRACT

Inkjet printing is a scalable technique that can fabricate customised three-dimensional microstructures, reproducibly, accurately, and with high material utilisation, by printing multiple layers sequentially onto previously printed layers, to produce architectures tailored in this case to electrochemical reactors.

Printable yttria-stabilised zirconia (YSZ) and lanthanum strontium manganite (LSM) inks were formulated to enable fabrication of solid oxide electrochemical reactors (SOERs): H_2O-H_2 | Ni(O)-YSZ | YSZ | YSZ pillars | LSM | O_2. Of the geometries studied, equi-sized, hexagonally-arranged cylindrical pillars were predicted to produce the largest ratio of interfacial to geometric (cross-sectional) areas. However, this neglects effects of potential and current density distributions that constrain up-scaling to more modest factors. Hence, using kinetic parameter values from the literature, finite element computational simulations of the pillared SOER in (H_2 - O_2) fuel cell mode predicted peak power densities of 0.11 W cm^{-2} at 800 °C, whereas its counterpart with only a planar electrolyte layer produced only 0.05 W cm^{-2}; i.e. the pillars were predicted to enhance peak power densities by ca. 2.3.

Arrays of several thousand YSZ cylindrical pillars were printed, with post-sintering diameter, height, and spacing of 25, 95 and 63 μm, respectively. LSM was inkjet-printed onto the pillars, and sintered subsequently, to produce contiguous films *ca.* 4 μm thick. In (H_2 - O_2) fuel cell mode at 725, 770, and 795 °C, these reactors produced peak power densities of 0.09, 0.21, 0.30 W cm^{-2}, respectively, 3–6 times greater than the performance of 'benchmark' Ni(O)-YSZ | YSZ | LSM reactors inkjet-printed with planar cathodes operating under the same conditions, thereby demonstrating the benefit of inkjet printing as a fabrication technique for SOERs.

1. Introduction

Solid oxide fuel cells (SOFCs) are an attractive chemical-to-electrical energy conversion technology, operating at 550-850°C [1–3] with high energy efficiencies (*ca.* 90%) [4] depending on current density, and not requiring precious metal catalysts, unlike alkaline and polymer electrolyte fuel cells. SOFC electrodes are fabricated conventionally by powder mixing methods, resulting in unpredictable microstructures and hence unpredictable densities of triple phase boundaries (TPBs) [5–8], *i.e.* the intersections of ionically (io) and electronically (el) conducting phases with pores (p). All three phases must be percolating to sustain electrochemical reactions, exemplified by reactions (1) and (2), respectively, for the anode and cathode of a hydrogen-oxygen fuel cell:

$$H_{2(p)} + O^{2-}_{(io)} \rightarrow H_2O_{(p)} + 2e^-_{(el)} \quad (1)$$

$$O_{2(p)} + 4e^-_{(el)} \rightarrow 2O^{2-}_{(io)} \quad (2)$$

Typically, yttria-stabilised zirconia (YSZ) is used for the ionically-conducting phase, nickel and lanthanum strontium manganite (LSM) for the electronically-conducting phase for the negative and positive electrodes, respectively, with pores enabling supply / removal of gaseous reagents / products (*i.e.* H_2, H_2O, O_2). Focused Ion Beam (FIB) – SEM experiments have found that within conventionally-fabricated electrodes, the TPB density, fraction of TPBs that are percolated, and microstructure for identical composition vary significantly, as shown in Table 1. Therefore, by increasing the fraction of percolating TPBs, it should be possible to increase electrode performance.

Inkjet printing is a scalable fabrication technique that has been used previously to fabricate reproducibly the electrolyte [14–17] and conventional composite electrodes for solid oxide fuel cells and electrolysers (Solid oxide electrochemical reactors, SOERs) [18–23]. However, the

* Corresponding author.
E-mail address: i.jang@imperial.ac.uk (I. Jang).
ISE member

https://doi.org/10.1016/j.electacta.2022.140834
Received 30 December 2021; Received in revised form 28 May 2022; Accepted 9 July 2022
Available online 12 July 2022

Nomenclature

Symbol	Definition	Units
$W(T)$	work done on the electrode during sintering at temperature (T)	J
γ_{LSM}	surface energy of LSM	J m^{-2}
ΔA_{LSM}	average change in surface area	m^2
δr	circular annulus thickness	m
$N(r)$	number of particles within the annulus	1
ΔV	total volume of annulus	m^3
V_{LSM}	volume of individual LSM particle	m^3
φ	particle volume fraction in the dried film	1
H	film depth	m
$r_{p.0}$	particle radius at pre-sintering conditions	m
r	radius of pillar from outer diameter	m
π	pi, 3.14159	1
U	cell potential difference	V
ϕ	electrode potential	V
E	electrode potential vs. reference electrode	V
η	overpotential	V
j	current density	A m^{-2}
d	current path length	m
σ	conductivity	S m^{-1}
C	capacitance	F
R	resistance	Ohm
p	power density	W m^{-2}
∇	$\frac{\partial}{\partial x}+\frac{\partial}{\partial y}+\frac{\partial}{\partial z}$,	
∇^2	$\frac{\partial^2}{\partial x^2}+\frac{\partial}{\partial y^2}+\frac{\partial}{\partial^2 z}$,	

Table 1
Porosity and fraction of non-percolating TPBs for different electrodes.

Electrode Material	TPB density / μm μm^{-3}	Non-percolating fraction of TPBs / %	Porosity / %	Refs.
YSZ-LSM	7.35	28 – 43	52	[7]
YSZ-LSM	Not provided	Not provided	43	[9]
YSZ-LSM	4.35	Not provided	36	[10]
YSZ-LSM	6.6 - 8.3	9 – 13*	34	[11]
Ni-YSZ	4.28	37	19.5	[8]
Ni-YSZ	2.56	35 – 58	48.8	[12]
Ni-YSZ	3.06	6	23	[13]
YSZ-LSM	10.24	34	50.6	[13]

* Depending on characterisation method.

fraction of percolating TPBs within these electrodes is not expected to differ significantly from conventionally-fabricated electrodes, because they also were derived from composite powder-mixing methods. Rather than printing particle composite electrodes, inkjet printing can be utilised for defining TPBs by depositing the ionically and electronically-conducting phases sequentially. Moreover, when the 3D electrolyte microstructures were inkjet printed, not only is conformal coating of porous electrode layers on the structure enabled, but also larger electrolyte | electrode interfacial areas are achieved for a given geometric area, allowing synergistic effects of 3D structures and porous microstructures of electrodes in SOERs. Hence, the fraction of percolated TPBs can be increased, by ensuring each phase is contiguous, and by tailoring the electrode microstructure; the enhanced interfacial area between each phase can be predicted precisely as explained in Section 2 below.

2. Calculations of total and 'Active' electrolyte | electrode areas

2.1. Electrolyte | electrode interfacial areas for electrolytes with pillars and cones

The up-scaled three-dimensional electrolyte | electrode areas are shown in Fig. 1, for cylindrical pillar arrays that could be inkjet-printed with a demonstrated inkjet printer lateral resolution (droplet spread diameter) of 25 μm [14], at which the pillar diameter in the calculation was also fixed. As inkjet printing is a layer-by-layer deposition technique, the smallest feature possible is a droplet, which ultimately results in circular deposition; hence, many droplets deposited sequentially on top of each other necessarily produce a cylinder. Evidently, as shown in Fig. 1b, hexagonal arrays of cylindrical pillars are predicted to increase the electrode | electrolyte interfacial area most effectively, and hence their electrode TPB density should be greatest.

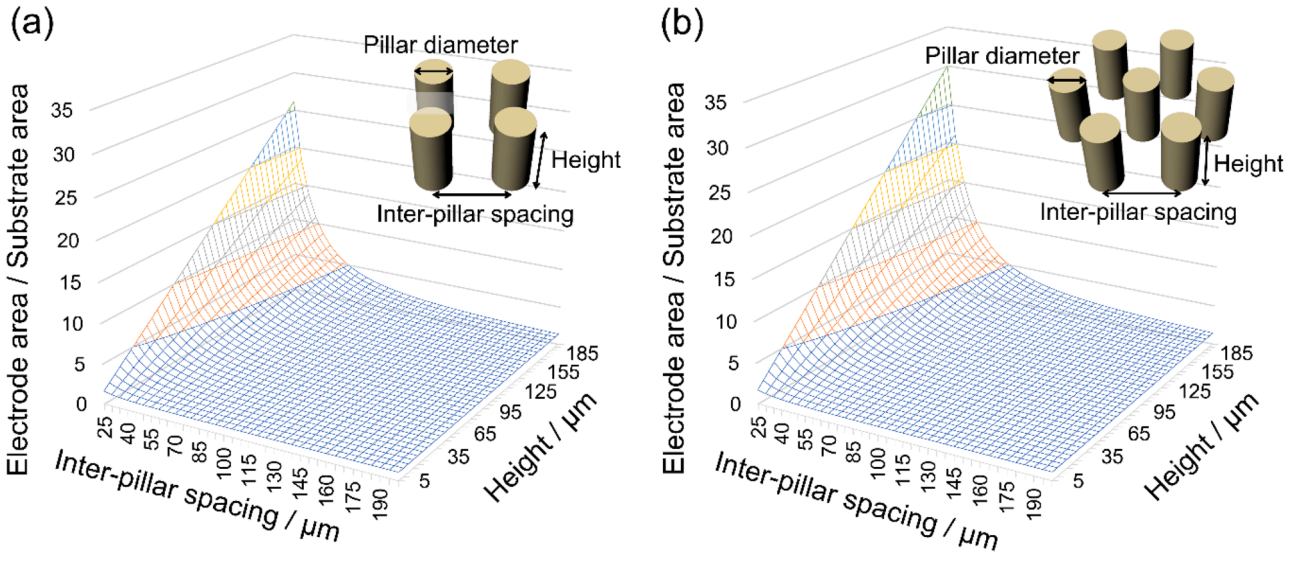

Fig. 1. Interfacial area enhancement for different three-dimensional structures, constrained by a minimum lateral feature resolution of 25 μm for: (a) cylindrical pillars in a square array; and (b) cylindrical pillars in a hexagonal array.

2.2. Primary potential and current distribution in pillars

Pillared electrolytes on top of planar electrolyte imply increasing current path lengths and hence decreasing current densities with increasing pillar height. Fig. 2 shows the primary (2D) potential distribution in the planar and pillared electrolyte, with the potential gradient just below the (single) pillar being less than that in the rest of the planar electrolyte, in which greater current densities are predicted. Hence, for the case of infinitely fast interfacial kinetics, zero overpotential, current densities into or out of the pillar are predicted to be less than in the rest of the planar electrolyte, so the pillar would then have a negative effect on the global reactor performance.

For the case of planar electrolyte with a single pillar of electrolyte on top, Fig. 3a shows a schematic equivalent electronic circuit, for an operating potential difference U, between the potentials of positive (ϕ_p) and negative electrodes (ϕ_n) due to ohmic potential losses at current density j_i over path length d_i and conductivity σ_i in phase or domain i. As the current path length d_i is larger for the pillar than the planar electrolyte, but the ohmic potential component ($j_i d_i/\sigma_i$) of the potential difference U and the thermodynamic potential difference (E_p - E_n) are constant, the local current density j_i for the pillar must scale inversely with path length, so must be less than that in the planar electrolyte.

When finite overpotentials / reaction impedances are considered at electrolyte | electrode interfaces, as shown schematically in Fig. 3b, their effect is to partially homogenise ('secondary') current distributions, but at the expense of increased potential differences at fixed overall current, due to additional potential losses in reaction impedances. Hence, unlike for the primary current distribution, depending on current densities, electrode kinetic parameters, and electrolyte ohmic resistance, and so on pillar geometries, reaction impedances may become the most significant contribution to the overall reactor resistance. The slower the kinetics, the more current flows in the pillared electrolyte, increasing 'active' areas, so the more effective the pillars will be in enhancing a reactor's global performance. However, increased reaction impedances increase reactor potential differences at constant current (or decrease global currents at constant potential difference), decreasing energy conversion efficiencies and increasing operating costs (OPEX). Hence, optimisation is required to minimise (CAPEX + OPEX) costs, as the greater the active area per geometric area by judicious selection of printed geometries, the lower the capital costs (CAPEX).

Non-linear reaction kinetics require computational solutions of the resulting spatial current density distributions, as described in Section 2.3; experimental results reported in Section 4.2 demonstrate the beneficial effects of pillars in enhancing reactor performances.

2.3. Computational simulations of secondary / tertiary potential and current distributions

Comsol FEM software was used to solve Laplace's equation ($\nabla^2\phi = 0$) in 3D, with the non-linear boundary conditions imposed by the interfacial kinetics.

Fig. 4a shows simulated potential difference-current-power density (U-j-p) data for the planar and the pillar structure model (a single cylindrical pillar in square symmetry boundaries) SOFCs at 800°C, with peak power densities of 0.05 and 0.11 W cm^{-2} respectively. These values correspond to a performance increase by a factor of ca. 2.3 for the model (square array) pillar structure compared to the corresponding planar structure. Unlike the case of the primary potential and current density distributions (Fig. 2), the finite faradaic impedance relative to the electrolyte resistance causes current to penetrate the pillar, so part of its area is utilised, though local current densities decay with increasing height, as shown in Fig. 4c.

Hence, when fabricating pillar structures, it is crucial to determine optimal pillar heights, with respect to both electrochemical performance and material costs. As shown in Fig. 4c, the active area in the pillar structure was concentrated mostly at the bottom of the pillar due to the increasing ohmic potential loss in the YSZ electrolyte pillar with increasing height. Results of computational simulations of the optimal electrode geometries and microstructures, will be reported in a future publication.

2.4. Project objectives

The project's two objectives were: (i) to determine whether or not, by depositing the conducting phases sequentially to fabricate hexagonal arrays of cylindrical pillars, three-dimensional SOFC cathodes with localised TPBs could be fabricated by inkjet printing, and with a greater fraction of percolating TPBs compared to conventional composite

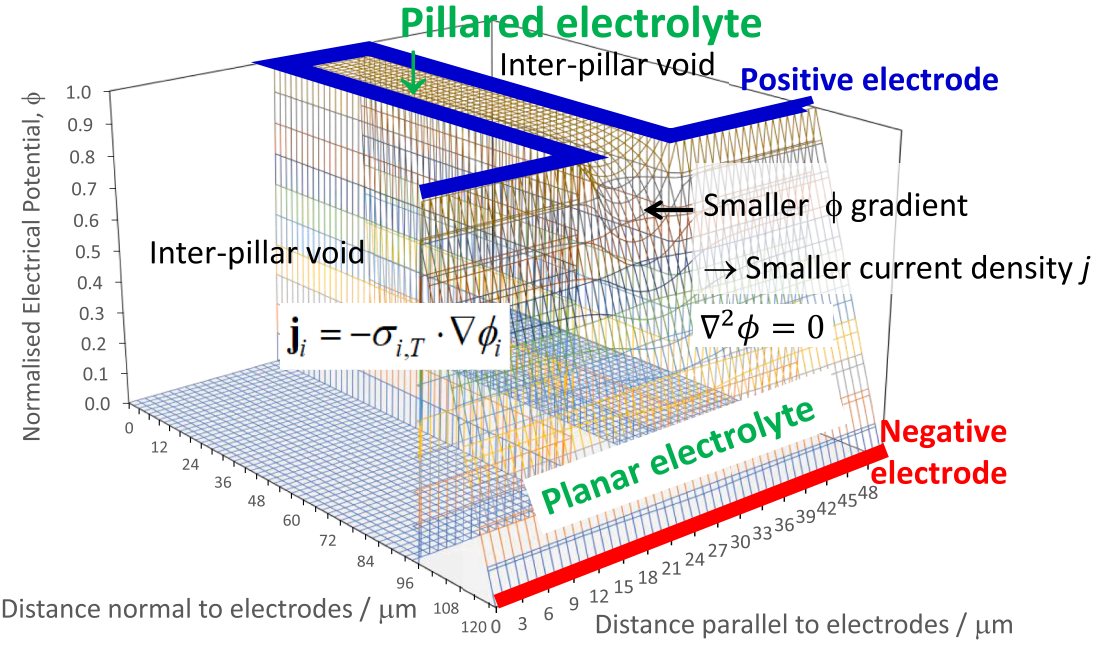

Fig. 2. Finite difference solution of Laplace's equation for the spatial distribution of the normalised 'primary' potential (ϕ) in the (planar + single pillar) electrolyte domain, with boundary conditions: ϕ(negative electrode) = 0, ϕ(positive electrode) = 1.

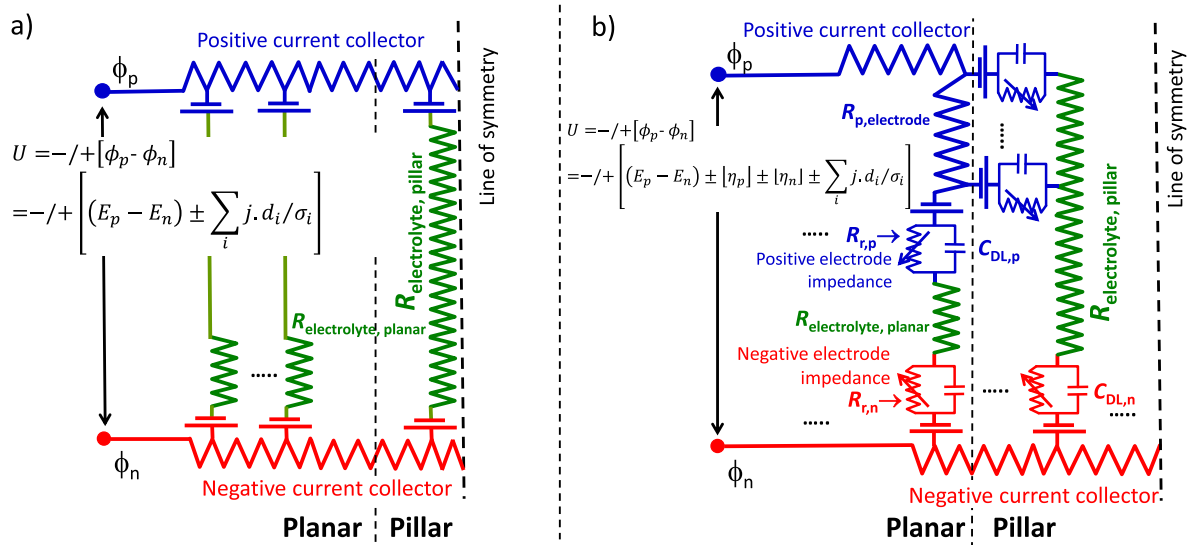

Fig. 3. Schematic equivalent electronic circuits for: (a) primary potential distribution, with infinitely fast kinetics and transport rates (zero overpotential); (b) secondary potential distribution, with finite electrolyte | electrode interfacial impedance. For positive and negative electrode reactions, potential source symbols (||) represent equilibrium potentials and RC symbols represent reaction impedances. Positive signs in square brackets of equations for electrolyser mode (*U* negative, so ΔG positive by convention) and negative signs for fuel cell mode (*U* positive, so ΔG negative by convention).

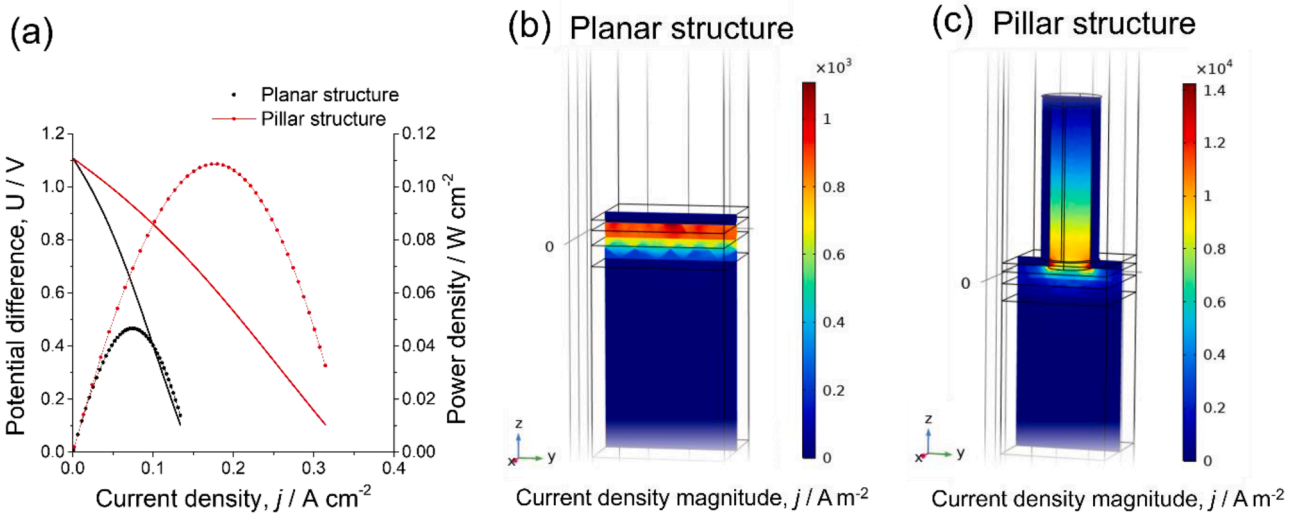

Fig. 4. (a) Predicted *U-j-p* global performances of solid oxide fuel cells with planar and pillar structures (in square symmetry boundaries) at 800 °C, and predicted current density distributions through YSZ electrolyte in (b) planar structure and (c) pillar structure, at 0.5 V potential difference.

electrodes; and (ii) to demonstrate that the electrochemical performance of those electrodes is superior to that of planar YSZ | LSM electrodes, as predicted by the results shown in Fig. 4.

Herein, we report the modelling and fabrication of pillared YSZ-LSM cathodes for SOFCs with the structure Ni-YSZ | YSZ | YSZ pillars | LSM and the corresponding planar structured SOFCs by inkjet printing, as shown in Fig. 5, to compare their structural effects on the electrochemical performance in fuel cell mode.

3. Experimental

3.1. Fabrication of pillar and planar electrolyte structured cells

A NiO-YSZ electrode support layer was fabricated as outlined previously [18]. To fabricate the electrolyte, a Ceradrop X-Serie (Limoges, France) drop-on-demand piezoelectric inkjet printer with a Dimatix Sapphire printhead (30 pL nominal droplet volume, Fujifilm, USA) was used to deposit 10 layers of the aqueous YSZ ink formulation reported previously [18] at a droplet ejection frequency of 1100 Hz and overlap of 30% onto the NiO-YSZ support. Immediately after depositing the planar YSZ electrolyte, a hexagonal array of YSZ pillars 100 layers tall were deposited on top; the ejection frequency was reduced to 180 Hz to minimise unpredictable droplet drift after ejection (Fig. S1) which would cause defects in printed structures. This step was omitted for the planar YSZ|LSM 'benchmarking' SOFCs. The droplet ejection piezoelectric potential difference profile for the YSZ ink was a rise to 40 V over 1.5 μs, remaining at 40 V for 5 μs, and a decrease back to 0 V over 2.5 μs. The NiO-YSZ | YSZ | YSZ (pillars) structure was co-sintered at 1450°C for 5 h (Elite Thermal Systems, UK), with a dwelling step at 600°C to ensure all organic species were combusted completely.

A lanthanum strontium manganite ($La_{0.8}Sr_{0.2}MnO_3$, LSM, Fuel Cell Materials, USA) ink was formulated by dispersing LSM particles in butanol, stabilised colloidally by polyvinyl butyral (PVB, Butvar 98, Sigma Aldrich, USA), then centrifuged at a relative centrifugal force of

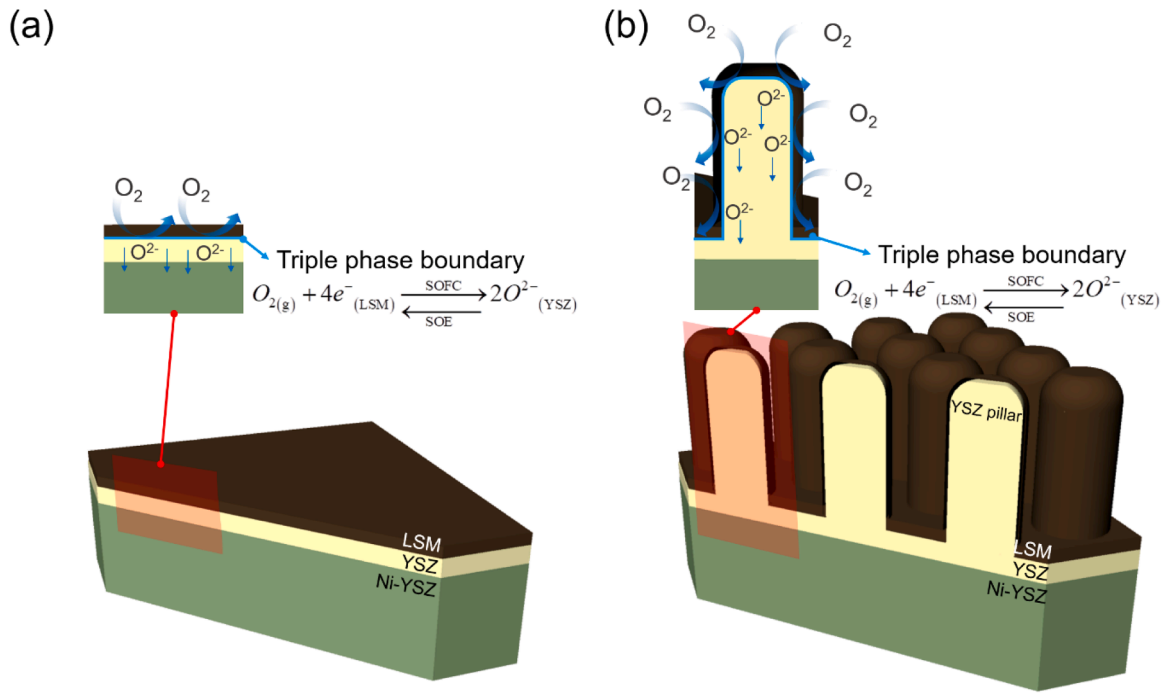

Fig. 5. Schematic illustration of the two SOFC geometries fabricated: (a) planar structure without pillars, and (b) pillared structure with enhanced electrode | electrolyte interfacial area.

1200 for 8 min to narrow the particle size distribution, then filtered with a syringe filter (800 nm aperture, Cole Parmer, UK) and concentrated to 12 wt% LSM. The final PVB mass fraction was 1.7 wt%. The LSM particle size and specific area have been reported previously [18]. The LSM ink was printed with a splat diameter of 80 μm and droplet overlap of 30% onto the sintered YSZ pillar array using a Fujifilm DMC (USA) 10 pL nominal droplet volume printhead with the droplet ejection profile: 0 to 50 V over 1 μs, remaining at 50 V for 7 μs, a decrease to – 50 V over 2 μs, remaining at – 50 V for 7 μs, and finally an increase back to 0 V over 1 μs.

For the YSZ ink formulation, YSZ particles (YSZ8-U1, Fuel Cell Materials, USA) were dispersed in de-ionised water, adding PMMA ammonium salt (Dispex A40, Ciba-BASF, UK;) as dispersant with a ratio of 0.2 mg m^{-2} to YSZ particle surface area value. Sonication and 24 h of stirring followed, then the ink was centrifuged to obtain a narrow particle size distribution, and filtered using a 800 nm size filter. After adding polyethylene glycol 35,000 (PEG 35000, Sigma Aldrich, USA) at 250 mg per 10 cm^{-3} to adjust the viscosity, the ink was stirred again for 24 h. Then alcohol ethoxylate (Natsurf 265, Croda Chemicals, UK) was added to adjust the surface tension as a final step to adjust the surface tension. More detailed conditions for formulating YSZ ink were published previously [14]; characterisations and optimisation of YSZ and LSM inks also were reported previously [18]. All printed layers were dried in air at 25°C; the structure was subsequently sintered at 1100°C for 3 h, with an intermediate dwelling step at 600°C to ensure all organics were combusted. LSM layers were printed with 15 layers on both planar and pillar structured cells prior to determination of their electrochemical performances. Additionally, 60 layers were printed on the pillar structure to compare the effect of LSM thickness on the layer properties after sintering. The 15 and 60 layers of printed LSM on the pillar array corresponded to ca. 4 μm and ca. 10 μm thicknesses, respectively, and 15 layers of printed LSM on the planar structure were ca. 6 μm thick. In the fabrication of both planar and pillar structures, the same amount of ink was used for coating planar YSZ electrolytes and LSM layers, the same number of layers being printed in the same defined area, in both geometries.

3.2. Electrochemical / material characterisation

Current collection was facilitated by Ag wires | Ag mesh | Ag wool (Alfa Aesar, UK), cemented to the cell using Ceramabond 552 (Pi-kem, UK). The cell was mounted on the open end of an alumina tube (Almath Crucibles, UK) to separate the gas mixtures at the anode and cathode, using the same ceramic adhesive, and cured at 94°C for 2 h, then at 260°C for 2 h. Prior to electrochemical measurements, the NiO electrode was reduced to Ni in hydrogen (flow rate 30 cm^3 min^{-1} throughout) for 24 h at 670°C. At sequentially increasing temperatures of 725, 770, and 795°C, electrochemical impedance spectroscopic measurements in 4 probe mode were made at the open circuit potential difference (OCPD) with a p-p amplitude of 10 mV between 10^5 and 10^{-1} Hz with ten points per frequency decade, and then while cycling the cell potential difference from the OCPD to 0.4 V at 5 mV s^{-1}. The cathode was exposed to air throughout.

All SEM photomicrographs were taken with a Hitachi TM3030 (Japan) with 15 kV beam energy, to verify the thicknesses of printed layer components and the microstructure of pillar arrays.

3.3. Computational simulations

COMSOL Multiphysics® version 5.6 software was used for finite element simulations of the electrochemical performance of both the cell with planar geometry, as shown in Fig. 5a: *Planar structure*, and the cell with cylindrical YSZ electrolyte pillars on a flat 7.5 μm YSZ electrolyte layer and covered with a 5 μm LSM electrode layer, as shown in Fig. 5b: *Pillar structure*. The pillar structure model was designed as a computational prediction of a single cylindrical pillar with square symmetry boundaries, which is the simplest design to validate the effect of pillar structure. The pillars were designed with 25 μm diameter, 95 μm height and 63 μm inter-pillar spacing, as for the printed and sintered pillared structure. The geometrical data for the models is listed in Table S1; the material information and electrochemical kinetic parameter values used in the models are reported in Table S2. Most of the kinetic data were taken from results reported in the literature, for which reference numbers [24–27] are listed in Table S2. However, as described in the

supplementary information (Figs. S4 and S5), exchange current densities and charge transfer coefficient values for oxygen electrode reactions were derived from experiments with a symmetric cell. Conditions such as working temperature, gas species ratio, and gas pressures used for the computational simulations are listed in Table S3 in the supplementary information.

4. Results and discussion

4.1. Structural characterisation

Fig. 6 shows SEM photomicrographs of the YSZ pillar array before and after sintering. The pre-sintering pillar diameter, height, and spacing were *ca.* 34, 105, and 72 μm, respectively; the height of a single printed layer of YSZ within the pillars was *ca.* 1 μm. Evidently, there were no missing pillars in the printed array, demonstrating the high reproducibility of inkjet printing (Fig. 6b). After sintering, the diameter, height, and spacing had decreased to *ca.* 25, 95, and 63 μm, respectively, as shown by Fig. 6c. At the top of each pillar, there was a small indentation, presumably caused by a mild coffee staining effect that occurred during droplet drying. This was not expected to have a detrimental effect on electrochemical performance. Internally, the pillars were highly dense, as shown by Fig. 6d, which should facilitate O^{2-} ionic conductivity through the pillars. Additional microstructural characterization of printed YSZ pillar structures and YSZ electrolyte is shown in Fig. S6.

Fig. 7a shows a SEM photomicrograph of the Ni(O)-YSZ | YSZ | LSM structure immediately outside of the pillar array, after sintering and electrochemical characterisation. Evidently, the electrolyte was highly dense, *ca.* 7.5 μm thick, and well adherent to both electrodes. The printed LSM layer was porous and *ca.* 4 μm thick, corresponding to an individual printed layer thickness of *ca.* 115 nm, smaller than the LSM mean particle size because the surface coverage of a single printed layer was less than a monolayer of particles. The thickness of the LSM layer in the 'benchmark' SOFC was *ca.* 6 μm (Fig. S2). This was thicker than the LSM coating over the pillars, as the surface area was decreased over which the LSM layer was spread; however, the difference was not large enough to have an effect on ohmic losses through the LSM, or significantly inhibit oxygen diffusion to YSZ | LSM interfaces, where the TPBs are located.

Fig. 7b shows a top-down view of the pillar array, after breaking the cell for structural characterisation. Relatively large fissures can be seen in the LSM layer between the pillars, equidistant from adjacent pillars. These features were not observed in the printed and dried LSM films prior to sintering. Therefore, they are believed to have formed during the LSM sintering process as a result of the compressive force generated during sintering, which may be derived from the work (W) done on the electrode during sintering at temperature (T), given by Eq. (3).

$$W(T) = \gamma_{\mathrm{LSM}}(T) \sum \Delta A_{\mathrm{LSM}} \tag{3}$$

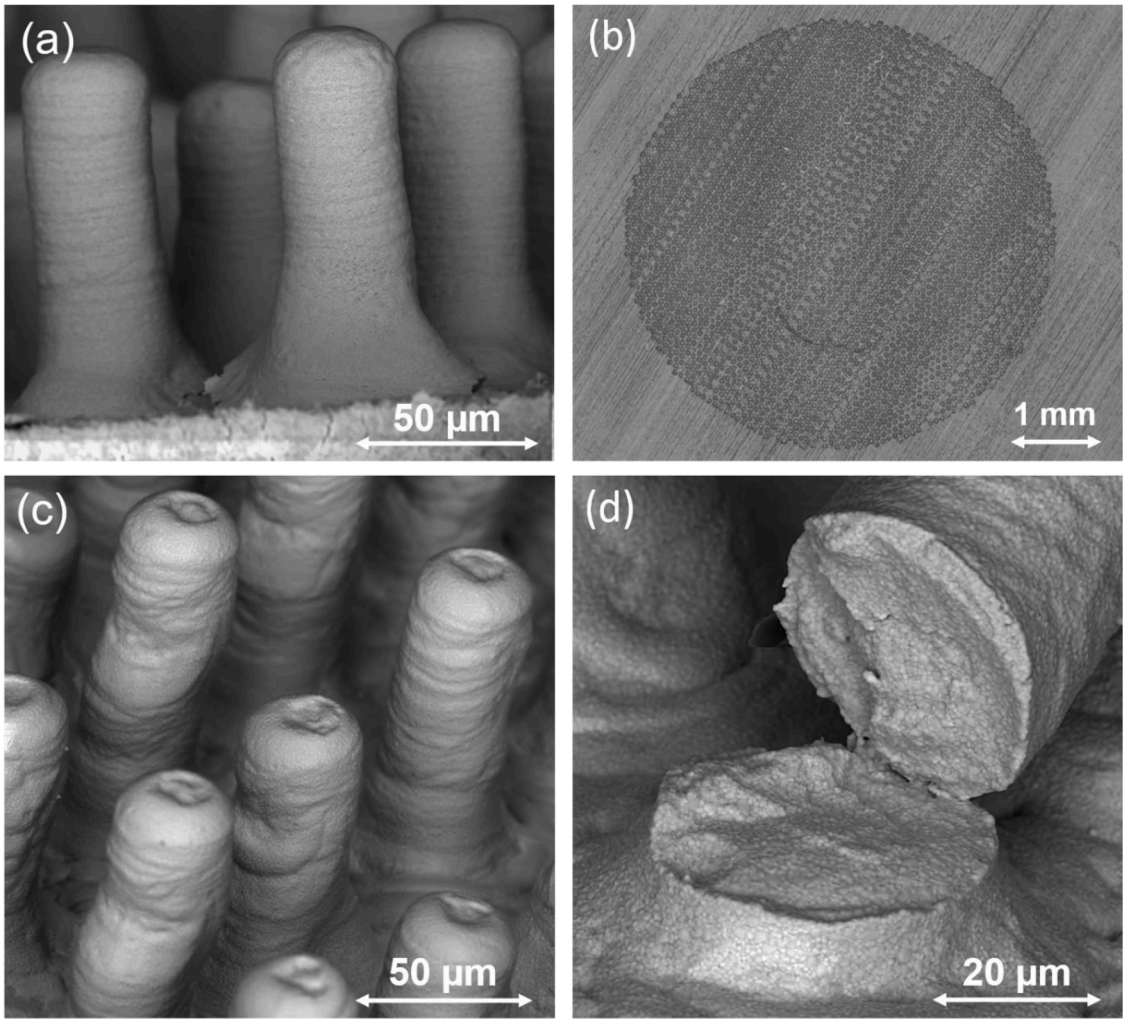

Fig. 6. Images showing the pillar array: (a) pre-sintering (SEM photomicrograph); (b) pillar array photograph; (c) post-sintering pillar array; (d) inside a broken pillar.

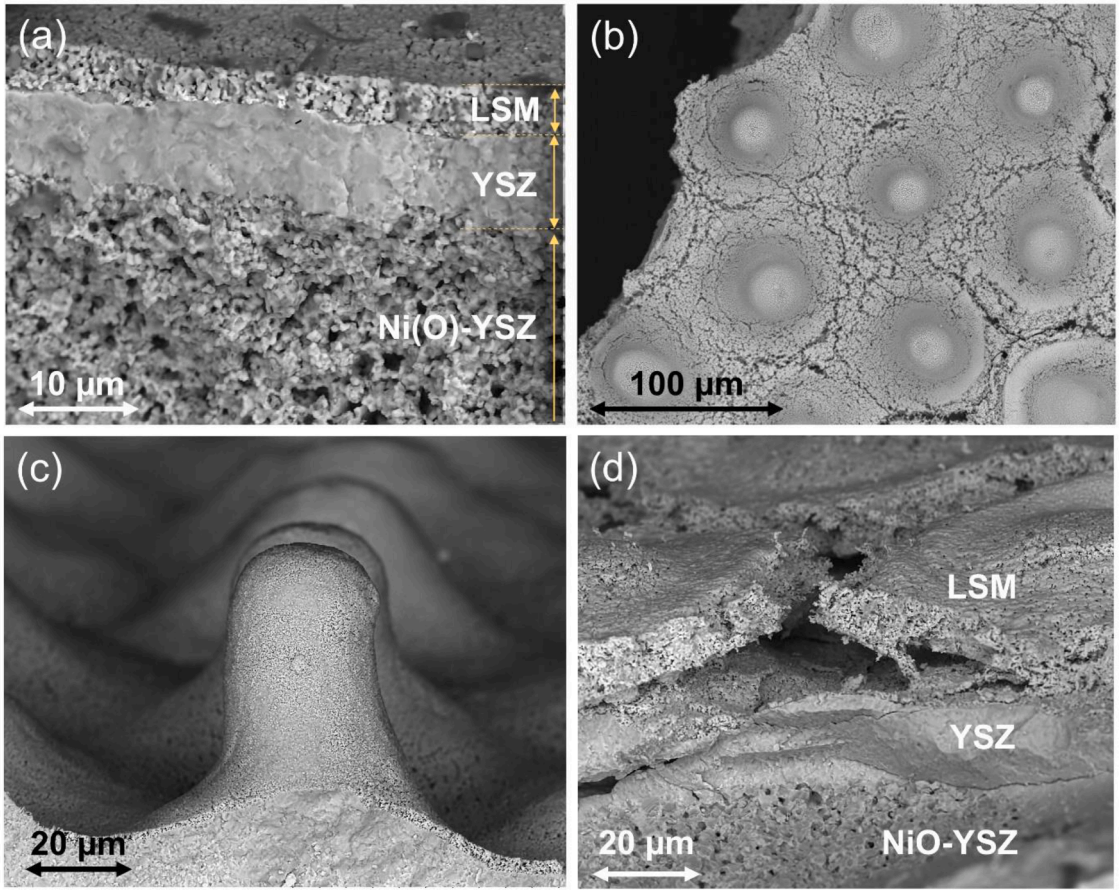

Fig. 7. SEM photomicrographs of: (a) cell structure away from the pillar array; (b) top-down view of the pillar array, after electrochemical characterisation; (c) 15 layers; and (d) 60 printed layers of LSM on the pillar array.

where γ_{LSM} represents the surface energy of LSM, and ΔA_{LSM} the average change in surface area of a LSM particle in the printed layer. Considering a circular annulus of thickness δr within the printed LSM film around a pillar positioned at radius r from the outer diameter of the pillar, Eq. (3) can be rewritten in terms of the work done within the annulus, as shown in Eq. (4).

$$\delta W(r,T) = \gamma_{LSM}(T) \times N(r) \times \Delta A_{LSM} \quad (4)$$

Where N(r) represents the number of LSM particles within the annulus and is equal to the total volume of particles divided by the volume of an individual LSM particle (V_{LSM}), as shown by Eq. (5), assuming no variation in θ, *i.e.* the film varies only radially.

$$N(r) = \frac{\varphi_0 \Delta V}{V_{LSM}} = \frac{2\pi r \delta r H_0 \varphi_0}{4/3\pi r_{p,0}^3} \quad (5)$$

where φ, H, and $r_{p,0}$ represent the particle volume fraction in the dried film, film depth, and particle radius at pre-sintering conditions ('0'), respectively. ΔV represents the volume of the annulus. Substituting Eqs. (5) into (4), the work done in the annulus can be derived, and is shown in Eq. (6):

$$\delta W(r,T) = \gamma_{LSM}(T).\varphi_0.\Delta A_{LSM}.\frac{3}{2}\frac{H_0}{r_{p,0}^3} r \delta r \quad (6)$$

Taking the limit $\delta r \to 0$, results in Eq. (7) for the (compressive) force during sintering, $F(r,T)$.

$$\frac{\delta W(r,T)}{\delta r} = F(r,T) = \gamma_{LSM}(T).\varphi_0.\Delta A_{LSM}.\frac{3}{2}\frac{H_0}{r_{p,0}^3} r \quad (7)$$

Therefore, with both increasing radial position and (initial) film height, the compressive force that occurs in the LSM film due to particle sintering increases linearly, which could explain the fissure formation during sintering, equidistant between adjacent pillars (axis of symmetry). Therefore, by decreasing the initial LSM film thickness and inter-pillar distance, the maximum compressive force should be decreased for identical printed particles. Evidence to support this hypothesis is in Fig. 7c and d, which show that when LSM thickness was decreased to 15 layers (Fig. 7c) fissures were not formed, and when LSM thickness was increased to 60 printed layers (Fig. 7d), fissures increased in size, ultimately causing delamination of the LSM film.

4.2. Electrochemical performance characterisation

After NiO reduction with hydrogen, the open circuit potential differences (OCPDs) at 725, 770, and 795°C were 1.147, 1.149, and 1.135 V, respectively, which are close to theoretically predicted values [4], indicating that the electrolyte and sealant were essentially gas-tight. Fig. 8a shows a Nyquist plot for the pillar structured SOFC characterised in hydrogen, at OCPD. Fig. 8c shows the variation in cell potential difference U with current density j, and corresponding power densities (p); peak power densities at 725, 770, and 795 °C were 0.09, 0.21, 0.30 W cm^{-2} respectively. These were *ca.* 3 (at 725 °C) – 6 (at 795 °C) times greater than the power densities of the benchmark cells, as shown in Fig. 8d, demonstrating that the pillars enhanced the electrochemical performance due to the greater number of TPBs, as implied by the significantly smaller cell polarisation shown in Fig. 8a compared to Fig. 8b. Compared to the *j-U-p* measurements of the planar SOFC (benchmark cell) with LSM electrode layer in other publications [28–30], the performance of the SOFC with a pillared structure in this study demonstrated explicitly an enhanced performance. This measured

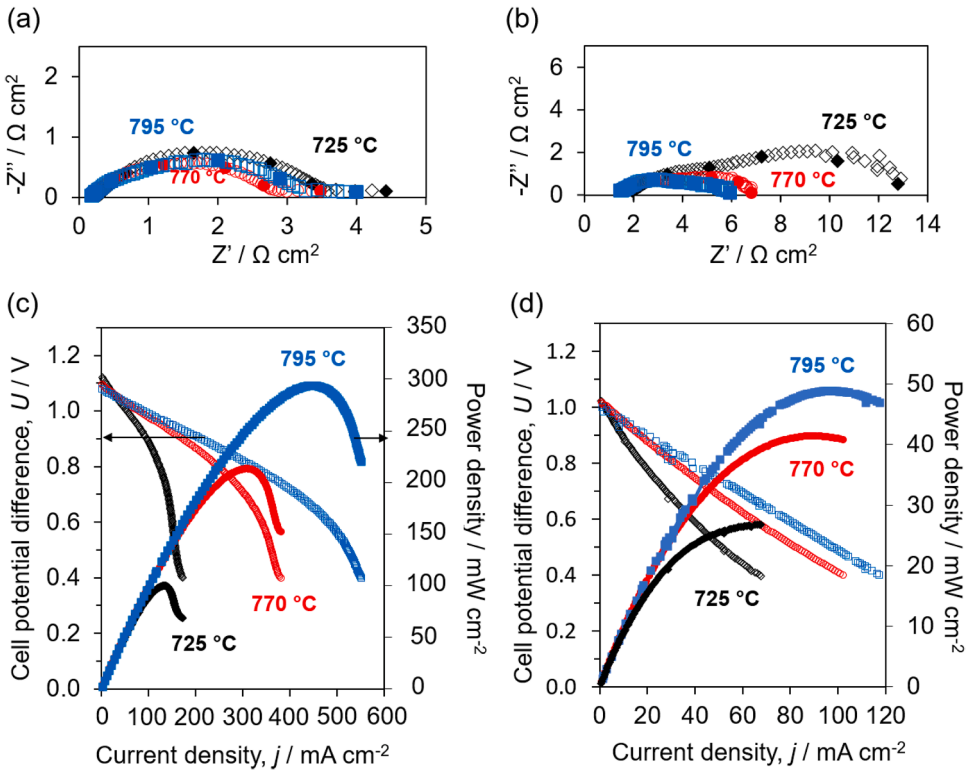

Fig. 8. Nyquist plots at OCPD of (a) H_2 | Ni(O)-YSZ | YSZ | YSZ (pillars) | LSM | air, (b) H_2 | Ni(O)-YSZ | YSZ (planar) | LSM | air, filled markers indicate frequency decades; effect of current density (j) on cell potential difference (U) (hollow markers) and power density (filled markers) of (c) the pillar structured SOFC, (d) 'benchmark' planar SOFC.

electrochemical performance increase was additionally supported by the computational simulations, which predicted ca. 2.3 times greater power densities at 800 °C, a similar performance enhancement factor. Considering that calculation was designed with a single cylindrical pillar with square symmetry boundaries, the enhancement factor could be even closer to the value obtained from the experimental performance. At lower temperatures, the effect of additional area of the pillars was decreased more than at higher temperatures. This was a consequence of spatial potential distributions within electrodes, which result from the temperature-dependent YSZ conductivity that is decreased at low temperatures, explaining why the performance enhancement was lowest at 725 °C. Evidently, electrochemical performance enhancement was non-linear with increasing pillar height, as implied by Fig. 4c. Therefore, to predict how electrochemical performance varies with electrode geometry, and hence to predict the optimal electrode geometry, requires numerical simulation of electrochemical kinetics, coupled with mass transport models.

As shown by Fig. 8a and b, unsurprisingly, the high frequency intercept decreased with increasing temperature, due to the increased YSZ conductivity. In the Nyquist plots for the pillar structured SOFC, the measured ohmic resistances were 0.29 Ω cm^{-2}, 0.21 Ω cm^{-2}, and 0.17 Ω cm^{-2} at 725°C, 770°C, and 795°C, respectively, and the polarisation resistances were 3.19 Ω cm^{-2}, 2.74 Ω cm^{-2} and 3.35 Ω cm^{-2} at 725°C, 770°C, and 795°C, respectively. The Nyquist plots of the planar SOFC exhibited ohmic resistances of 1.91 Ω cm^{-2}, 1.49 Ω cm^{-2}, and 1.44 Ω cm^{-2}, at 725°C, 770°C, and 795°C, respectively, and its polarisation resistances were 10.93 Ω cm^{-2}, 5.25 Ω cm^{-2} and 4.43 Ω cm^{-2} at 725°C, 770°C, and 795°C, respectively. At 795°C, at frequencies < 50 Hz, the cell impedance was greater than at 770°C, contrary to expectations, as mass transport impedances, which dominate at those characteristic times, are expected to diminish at higher temperatures [31–33]. Additional structural investigation of the post-characterised cells indicated that after exposure to high temperatures, the silver present in the current collector sintered to the top of the pillars (where the current collector was located), blocking reaction sites, and hence increasing mass transport impedances, as shown by the SEM photomicrographs in Fig. 9.

Despite hindering oxygen transport to the TPBs at the top of the pillar, Fig. 8c shows that the electrochemical performance at 795°C was greater than at 770°C, at which the Ag sintering coverage was less extensive. This is another consequence of the comparatively low conductivity of YSZ relative to LSM, causing significant spatial overpotential distributions within the electrode. Consequently, the most electrochemically active TPBs are those closest to the planar electrolyte, *i.e.* those furthest from the current collector and so less covered by Ag sintered to the LSM. In this case, the electrochemical characterisation occurred over *ca.* 48 h., so over longer times, this problem would be exacerbated; hence, Ag should be replaced with a more thermally-stable current collecting material, such as gold or platinum.

Fig. 8c shows that at current densities < ca. 0.1 A cm^{-2}, cell performance was dominated by ohmic potential losses, but at ca. 0.6 V, the resistance increased due to the onset of mass transport control, which become dominant at lower potential differences. However, the effect was not evident with planar cells, especially at 725°C and 770°C and current densities were low fractions of those of cells with pillar structures, possibly due to the relatively low TPB density at the cathode part of the planar structure, limiting the oxygen reduction kinetics. LSM is known to have variable oxygen stoichiometry depending on operating conditions [25], which may activate a bulk oxygen conduction pathway [26], creating oxygen vacancies in the LSM [27], enhancing oxygen transport rates to TPBs.

5. Conclusions

Inkjet printing of a colloidal YSZ ink was used to fabricate hexagonally-arranged cylindrical pillar arrays of YSZ electrolyte on NiO-YSZ substrates. LSM was inkjet printed on top of the sintered pillars, to

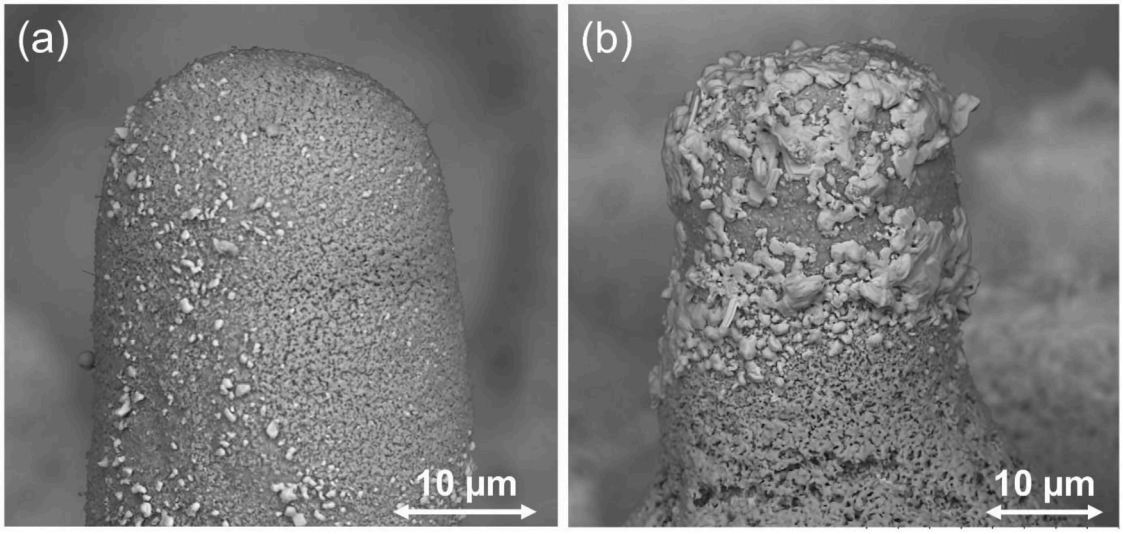

Fig. 9. SEM photomicrographs showing Ag from the current collector sintered to pillars that had been exposed to (a) 725°C; and (b) 795°C, after electrochemical characterisation.

produce solid oxide fuel cell (SOFCs) with structures: Ni(O)-YSZ | YSZ | YSZ pillars | LSM. Due to compressive forces that result from the decrease in particle surface area during sintering, decrease of the LSM film thickness was required to produce a film that adhered to the YSZ electrolyte and pillars without detaching.

Electrochemical characterisation of the resulting SOFCs at 725, 770, and 795 °C indicated that the electrolyte was gas-tight; peak power densities operating with dry hydrogen were 0.09, 0.21, 0.30 W cm^{-2}, respectively, *ca.* 3 (at 725 °C) to 6 (at 795 °C) times greater than power densities from a 'planar' benchmark cell (Ni-YSZ|YSZ|LSM without pillars). This demonstrated that the additional interfacial area provided by the pillars did indeed enhance the SOFC performance, by a temperature-dependent factor, due to spatial distributions of potential and current density, resulting from a temperature-dependent conductivity ratio of ca. 10^4 between YSZ electrolyte and LSM electrode phases, the charge transfer kinetics between which is also temperature dependent. Therefore, predicting the optimal electrode microstructure requires complex multi-physics simulations, results of which will be reported in a future publication [34].

Computational simulations predicted peak power densities increased by a factor of about 3 as a result of extending electrolyte | electrode interfacial areas, exemplified by YSZ pillar arrays, compared with those of planar YSZ electrolytes. This was validated experimentally for the printed cells, implying that the pillared 3D structure effectively increased the number of reaction sites per geometric area, thereby increasing SOFC performance.

CRediT authorship contribution statement

N.M. Farandos: Conceptualization, Writing – original draft, Validation, Investigation. **I. Jang:** Writing – review & editing, Validation, Investigation, Formal analysis. **J.C. Alexander:** Writing – review & editing, Formal analysis. **G.H. Kelsall:** Conceptualization, Writing – review & editing, Supervision, Resources, Project administration, Funding acquisition.

Declaration of Competing Interest

The authors declare that they have no known competing financial interests or personal relationships that could have appeared to influence the work reported in this paper. The authors declare the following financial interests/personal relationships which may be considered as potential competing interests:Inyoung Jang reports financial support was provided by Shell Global Solutions International BV. Nick M. Farandos reports financial support was provided by Shell Global Solutions International BV. John C. Alexander reports financial support was provided by Shell Global Solutions International BV. Geoff H. Kelsall reports financial support was provided by Shell Information Technology International BV.

Acknowledgment

The authors thank Shell Global Solutions International B.V. for post-doctoral research associateships for NMF, JCA and IJ.

Supplementary materials

Supplementary material associated with this article can be found, in the online version, at doi:10.1016/j.electacta.2022.140834.

References

[1] R.M. Ormerod, Solid oxide fuel cells, Chem. Soc. Rev. 32 (2003) 17–28.
[2] S.Z. Golkhatmi, M.I. Asghar, P.D. Lund, A review on solid oxide fuel cell durability: latest progress, mechanisms, and study tools, Renew. Sust. Energy Rev. 161 (2022), 112339.
[3] M. Rafique, H. Nawaz, M. Shahid Rafique, M. Bilal Tahir, G. Nabi, N. Khalid, Material and method selection for efficient solid oxide fuel cell anode: recent advancements and reviews, IJER 43 (2019) 2423–2446.
[4] K. Huang, J.B. Goodenough, Solid Oxide Fuel Cell Technology, Woodhead Publishing in Energy, Cambridge, 2009.
[5] B. Kenney, M. Valdmanis, C. Baker, J. Pharoah, K. Karan, Computation of TPB length, surface area and pore size from numerical reconstruction of composite solid oxide fuel cell electrodes, J. Power Sources 189 (2009) 1051–1059.
[6] H.W. Choi, A. Berson, B. Kenney, J. Pharoah, S. Beale, K. Karan, Effective transport coefficients for porous microstructures in solid oxide fuel cells, ECS Trans. 25 (2009) 1341.
[7] J.R. Wilson, A.T. Duong, M. Gameiro, H.Y. Chen, K. Thornton, D.R. Mumm, S. A. Barnett, Quantitative three-dimensional microstructure of a solid oxide fuel cell cathode, Electrochem. Commun. 11 (2009) 1052–1056.
[8] J.R. Wilson, W. Kobsiriphat, R. Mendoza, H.Y. Chen, J.M. Hiller, D.J. Miller, K. Thornton, P.W. Voorhees, S.B. Adler, S.A. Barnett, Three-dimensional reconstruction of a solid-oxide fuel-cell anode, Nat. Mater. 5 (2006) 541–544.
[9] N.S.K. Gunda, H.W. Choi, A. Berson, B. Kenney, K. Karan, J.G. Pharoah, S.K. Mitra, Focused ion beam-scanning electron microscopy on solid-oxide fuel-cell electrode: image analysis and computing effective transport properties, J. Power Sources 196 (2011) 3592–3603.
[10] K. Miyoshi, T. Miyamae, H. Iwai, M. Saito, M. Kishimoto, H. Yoshida, Exchange current model for $(La_{0.8}Sr_{0.2})_{0.95}MnO_3$ (LSM) porous cathode for solid oxide fuel cells, J. Power Sources 315 (2016) 63–69.
[11] G.J. Nelson, W.M. Harris, J.J. Lombardo, J.R. Izzo, W.K.S. Chiu, P. Tanasini, M. Cantoni, J. Van herle, C. Comninellis, J.C. Andrews, Y. Liu, P. Pianetta, Y. S. Chu, Comparison of SOFC cathode microstructure quantified using X-ray

nanotomography and focused ion beam–scanning electron microscopy, Electrochem. Commun. 13 (2011) 586–589.
[12] M. Kishimoto, H. Iwai, M. Saito, H. Yoshida, Quantitative evaluation of solid oxide fuel cell porous anode microstructure based on focused ion beam and scanning electron microscope technique and prediction of anode overpotentials, J. Power Sources 196 (2011) 4555–4563.
[13] J.S. Cronin, Y.-c.K. Chen-Wiegart, J. Wang, S.A. Barnett, Three-dimensional reconstruction and analysis of an entire solid oxide fuel cell by full-field transmission X-ray microscopy, J. Power Sources 233 (2013) 174–179.
[14] N.M. Farandos, L. Kleiminger, T. Li, A. Hankin, G.H. Kelsall, Three-dimensional Inkjet Printed Solid Oxide Electrochemical Reactors. I. Yttria-stabilized Zirconia Electrolyte, Electrochimica Acta 213 (2016) 324–331.
[15] V. Esposito, C. Gadea, J. Hjelm, D. Marani, Q. Hu, K. Agersted, S. Ramousse, S. H. Jensen, Fabrication of thin yttria-stabilized-zirconia dense electrolyte layers by inkjet printing for high performing solid oxide fuel cells, J. Power Sources 273 (2015) 89–95.
[16] Z. Zhu, Z. Gong, P. Qu, Z. Li, S.A. Rasaki, Z. Liu, P. Wang, C. Liu, C. Lao, Z. Chen, Additive manufacturing of thin electrolyte layers via inkjet printing of highly-stable ceramic inks, J. Adv. Ceram. 10 (2021) 279–290.
[17] S. Anelli, M. Rosa, F. Baiutti, M. Torrell, V. Esposito, A. Tarancón, Hybrid-3D printing of symmetric solid oxide cells by inkjet printing and robocasting, Addit. Manuf., 2022, 102636.
[18] N.M. Farandos, T. Li, G.H. Kelsall, 3-D inkjet-printed solid oxide electrochemical reactors. II. LSM - YSZ electrodes, Electrochim. Acta 270 (2018) 264–273.
[19] D. Young, A.M. Sukeshini, R. Cummins, H. Xiao, M. Rottmayer, T. Reitz, Ink-jet printing of electrolyte and anode functional layer for solid oxide fuel cells, J. Power Sources 184 (2008) 191–196.
[20] R.I. Tomov, R. Duncan, M. Krauz, R.V. Kumar, B.A. Glowacki, Inkjet printing and inkjet infiltration of functional coatings for SOFC fabrication, E3S Web Conf. 10 (2016) 00098.
[21] G.D. Han, K.C. Neoh, K. Bae, H.J. Choi, S.W. Park, J.W. Son, J.H. Shim, Fabrication of lanthanum strontium cobalt ferrite (LSCF) cathodes for high performance solid oxide fuel cells using a low price commercial inkjet printer, J. Power Sources 306 (2016) 503–509.
[22] M.A. Sukeshini, R. Cummins, T.L. Reitz, R.M. Miller, Ink-Jet printing: a versatile method for multilayer solid oxide fuel cells fabrication, J. Am. Ceram. Soc. 92 (2009) 2913–2919.
[23] S. Kawale, I. Jang, N. Farandos, G.H. Kelsall, Inkjet 3D-printing of functional layers of solid oxide electrochemical reactors: a review, React. Chem. Eng. (2022).
[24] C. Zhang, C.J. Li, G. Zhang, X.J. Ning, C.X. Li, H. Liao, C. Coddet, Ionic conductivity and its temperature dependence of atmospheric plasma-sprayed yttria stabilized zirconia electrolyte, Mater. Sci. Eng. B 137 (2007) 24–30.
[25] S. Masciandaro, M. Torrell, P. Leone, A. Tarancón, Three-dimensional printed yttria-stabilized zirconia self-supported electrolytes for solid oxide fuel cell applications, J. Eur. Ceram. Soc. 39 (2019) 9–16.
[26] D. Das, R.N. Basu, Improved polarization behaviour of nanostructured $La_{0.65}Sr_{0.3}MnO_3$ cathode with engineered morphology, Int. J. Hydrogen Energy 42 (2017) 15347–15358.
[27] D. Cui, C. Yang, K. Huang, F. Chen, Effects of testing configurations and cell geometries on the performance of a SOFC: a modeling approach, Int. J. Hydrogen Energy 35 (2010) 10495–10504.
[28] Z. Jiang, L. Zhang, K. Feng, C. Xia, Nanoscale bismuth oxide impregnated (La, Sr) MnO_3 cathodes for intermediate-temperature solid oxide fuel cells, J. Power Sources 185 (2008) 40–48.
[29] G.B. Jung, C.T. Chang, C.C. Yeh, X.V. Nguyen, S.H. Chan, C.Y. Lin, J.W. Yu, W. T. Lee, S.W. Chang, I.C. Kao, Study of reversible solid oxide fuel cell with different oxygen electrode materials, Int. J. Hydrogen Energy 41 (2016) 21802–21811.
[30] W. Guan, H. Zhai, L. Jin, T. Li, W. Wang, Effect of contact between electrode and interconnect on performance of SOFC stacks, Fuel Cells 11 (2011) 445–450.
[31] D.A.G. Bruggeman, Berechnung verschiedener physikalischer Konstanten von heterogenen Substanzen. I. Dielektrizitätskonstanten und Leitfähigkeiten der Mischkörper aus isotropen Substanzen, Ann. Phys. 416 (1935) 636–664.
[32] B. Tjaden, S.J. Cooper, D.J.L. Brett, D. Kramer, P.R. Shearing, On the origin and application of the Bruggeman correlation for analysing transport phenomena in electrochemical systems, Curr. Opin. Chem. Eng. 12 (2016) 44–51.
[33] B. Todd, J.B. Young, Thermodynamic and transport properties of gases for use in solid oxide fuel cell modelling, J. Power Sources 110 (2002) 186–200.